SCIENCE CHINA
Technological Sciences

December 2011 Vol.54 No.12: 3265–3274
doi: 10.1007/s11431-011-4574-y

Numerical simulation of sandy bed erosion by 2D vertical jet

HUAI WenXin, WANG ZengWu, QIAN ZhongDong* & HAN YaQiong

State Key Laboratory of Water Resources and Hydropower Engineering Science, Wuhan University, Wuhan 430072, China

Received December 6, 2010; accepted June 12, 2011; published online November 5, 2011

A two-dimensional numerical model of vertical jet scour was developed based on the turbulent flow theory and jet scour mechanism. In this model, drag force acts as the main reference variable and the critical Shields number acts as the incipient motion criteria of sediment. The morphological change in the bed caused by bed-load transport is simulated using the moving mesh method and the suspended-load is not considered. An experiment investigating vertical clear water jet scour was conducted in the laboratory, and some effective experimental results, such as flow patterns and distribution characteristics of scour pits, were obtained. Numerical simulation of the 2D jet scour was conducted using the same parameters as were used in the flume experiment. The evolution process of the jet scour observed in the experiment was simulated by the new model; validation of the numerical model and the algorithm was conducted. Semi-empirical formulas of the characteristic length of the equilibrium scour hole were deduced based on the results of the experiment and simulation.

jet scour, numerical simulation, moving mesh, Shields number

Citation: Huai W X, Wang Z W, Qian Z D, et al. Numerical simulation of sandy bed erosion by 2D vertical jet. Sci China Tech Sci, 2011, 54: 3265–3274, doi: 10.1007/s11431-011-4574-y

1 Introduction

It is important to investigate the scour caused by downstream flow of rivers, because poor scouring design will lead to instability of structures constructed in rivers. The most serious problem with this phenomenon is local scouring in areas downstream of dams caused by water jets from bucket energy dissipation buildings, which is commonly known as jet scour. Jet scour is important in engineering of desilting facilities, water pipelines, water intake facilities and reservoirs. This is because the jets associated with these facilities can increase local turbulence intensity and improve the carrying capacity of water, which is useful for preventing sediment deposition or removal of sediment from the bed.

Local scour is divided into two categories, clear-water scour and live-bed scour. Clear-water scour occurs when the sediment concentration of the water is zero, otherwise live-bed scour occurs. Jets are classified as follows based on their shapes: plane (2D) jet, circular (axial symmetry) jet and rectangular (3D) jet [1]. Local jet scour has been extensively researched at home and abroad. Li et al. [2, 3] reported the geometrical similarity of scour holes and built empirical equations describing the characteristic length of scour holes based on experimental results. Westrich et al. [4] studied the scour of a homogeneous sand bed caused by a jet. Mih et al. [5] analyzed the factors that affected the scour depth and covering thickness, including nozzle diameter, outflow velocity, injection angle and scour distance. The researches conducted by Aderibigbe and Rajaratnam [6, 7] and Rajaratnam and Mazurek [8] showed that the max scour depth is dependent on density Froude number F_{rd}, scour distance h and nozzle diameter d_0. Yüksel et al. [9] investigated the local scour caused by a circular jet around pile groups and found that the density Froude number F_{rd}, the

---

*Corresponding author (email: zdqian@whu.edu.cn)

clearance ratio *a*/*D* and the size of the pile relative to the circular water jet diameter D/d_0 were the main factors affecting the scour around pile groups.

In recent years, numerical simulation has been widely used in studies of local scour. Based on potential-flow theory, Li et al. [10] proposed a mathematical model and simulated the scour hole around offshore pipelines. This model assumes that the shear force at the bed surface is not larger than the critical shear force when the scour equilibrium is reached, which is different from the traditional sediment transport model. Based on these assumptions, the seabed topography was calculated. Liang et al. [11] conducted 2D numerical simulation of local scour by steady flow in offshore pipelines, in which the bed deformation was simulated by moving mesh. A sand slide model was also developed. Comparison of computational results obtained using the Smagorinsky subgrid scale (SGS) model and $k-\varepsilon$ turbulence model indicated that the latter was more useful. Salaheldin et al. [12] simulated the scour around vertical circular piers in clear water using the CFD software, FLUENT. Roulund et al. [13] investigated the flow field and local scour around the circular pier experimentally and by 3D numerical simulation and described the process of scour hole deformation using moving mesh technology. Lu et al. [14] simulated local scour around submarine pipelines using the renormalized group (RNG) turbulence model based on the finite element method and unstructured triangle grid system. In Lu's paper, the incipient criterion for sediment was the critical shear stress based on the Shields parameter.

Liu et al. [15] simulated the motion of free water surface using the VOF method and calculated the water-sediment interface using the Lagrangian and moving mesh method, and found that the computational results agreed well with the experimental ones. Zhao and Cheng [16] solved RANS equations by the finite element method, simulated bed deformation by the mass conservation method and investigated local scour around a piggyback pipeline. Yüksel et al. [17] simulated vertical local scour around a circular pillar using a realizable k–ε turbulence model and obtained reasonable computational results.

In this study, 2D vertical jet scour was simulated based on turbulence theory. The RNG turbulence model was employed and the bed-load sediment was considered using sediment transport equations. There are many contributors to the transportation of sediment, and there is no perfect equation to describe this phenomenon, and the handy empirical equations all have certain application limits. The mathematic model proposed by Li and Cheng [18] was applied, in which sediment particles start to move only when the drag forces acting on them exceed a certain value. A bed-load sediment transport equation dependent on relative water shear stress (Shields number) was derived. In this new model, whether the relative shear stress (Shields number) reaches the threshold relative shear stress (threshold Shields number) or not is considered as the criteria of sediment incipient motion. Deformation of the scour hole is simulated by the moving-mesh method, and no traditional empirical formula is needed. Based on the numerical simulation and experimental study, the flow field characteristics and the geometrical similarity of the scour hole were obtained, then a semi-empirical formula for the characteristic length of the scour hole was built by dimensional analysis.

2 Hydrodynamic model

2.1 Flow model

The governing equations for the plane 2D jet fluid flow are the continuity equation and the momentum equation:

$$\frac{\partial u_i}{\partial x_i}=0, \tag{1}$$

$$\frac{\partial u_i}{\partial t}+u_j\frac{\partial u_i}{\partial x_j}=-\frac{1}{\rho}\frac{\partial P}{\partial x_i}+\frac{\partial}{\partial x_j}(2\nu S_{ij}-\overline{u_i'u_j'}), \tag{2}$$

where

$$S_{ij}=\frac{1}{2}\left(\frac{\partial u_i}{\partial x_j}+\frac{\partial u_j}{\partial x_i}\right), \tag{3}$$

$$\overline{u_i'u_j'}=\nu_T\left(\frac{\partial u_i}{\partial x_j}+\frac{\partial u_j}{\partial x_i}\right)+\frac{2}{3}k\delta_{ij}, \tag{4}$$

where u_i is the fluid velocity component in i direction, u_i' is the fluctuation of fluid velocity in i direction, P is the pressure, S_{ij} is the mean strain rate tensor, $\overline{u_i'u_j'}$ is the Reynolds stress tensor, ρ is the fluid density, ν is the fluid kinetic viscosity, ν_T is the turbulence viscosity, k is the turbulent kinetic energy, and δ_{ij} is the Kronecker delta ($\delta_{ij}=1$, $i=j$; $\delta_{ij}=0$, i=j).

2.2 Turbulence model

Recently, many improved k–ε models have been proposed by scientists and engineers based on the standard k–ε model. Yakhot and Orszag [19] developed a high Reynolds number k–ε model, named the RNG (renormalization group) k–ε model, in which the coefficients were not obtained from experimental data, but from theoretical analysis. The RNG k–ε model is used more widely than the standard k–ε model, especially for measurement of the fluid flow in the low intensity turbulence field and strong shear zone.

This study uses the RNG k–ε model to simulate the turbulent flow and the wall function is adopted for the wall. The equations for k and ε are

$$\frac{\partial k}{\partial t}+u_j\frac{\partial k}{\partial x_j}=\tau_{ij}\frac{\partial u_i}{\partial x_j}+\frac{\partial}{\partial x_j}\left[\frac{1}{\rho}\left(\mu+\frac{\mu_T}{\sigma_k}\right)\frac{\partial k}{\partial x_j}\right]-\varepsilon, \tag{5}$$

$$\frac{\partial \varepsilon}{\partial t}+u_j\frac{\partial \varepsilon}{\partial x_j}=C_{\varepsilon 1}\frac{\varepsilon}{k}\tau_{ij}\frac{\partial u_i}{\partial x_j}+\frac{\partial}{\partial x_j}\left[\frac{1}{\rho}\left(\mu+\frac{\mu_T}{\sigma_\varepsilon}\right)\frac{\partial \varepsilon}{\partial x_j}\right]-C_{\varepsilon 2}\frac{\varepsilon^2}{k}, \tag{6}$$

where k is the turbulent kinetic energy

$$k=\frac{1}{2}\overline{u_i'u_i'}, \tag{7}$$

θ is the dissipation of turbulent kinetic energy

$$\varepsilon=\nu\overline{\frac{\partial u_i'}{\partial x_k}\frac{\partial u_i'}{\partial x_k}}, \tag{8}$$

μ is the fluid viscosity and μ_T is the turbulent eddy viscosity:

$$\mu_T=C_\mu\rho\frac{k^2}{\varepsilon}, \tag{9}$$

$$\tau_{ij}=\frac{\mu_T}{\rho}\left(\frac{\partial u_i}{\partial x_j}+\frac{\partial u_j}{\partial x_i}\right)-\frac{2}{3}\rho k\delta_{ij}, \tag{10}$$

τ_{ij} is the Reynolds stress, and the constants in the RNG k–ε model are those defined in Table 1.

3 Sediment transport model

3.1 Bed-load model

In this study, only the bed-load sediment was considered and the sediment was uniformly non cohesive. The bed-load model used herein was similar to the model described by Chen [20].

There are five primary methods available for studying the bed-load sediment, flow velocity, drag force, energy balance, statistical law and sand wave movement [21]. This study employed the bed-load sediment transport rate formula dependent on drag force to study the bed-load sediment. This type of formula takes the drag force as the main factor when calculating the bed-load sediment transport rate. The sediment transport rate increases with the drag force.

Table 1 Constants in RNG g model

C_μ	$C_{\varepsilon 1}$	$C_{\varepsilon 1}$	σ_k	σ_ε
0.085	1.42	1.68	0.7179	0.7179

The drag force τ is defined as

$$\tau=\rho U_*^2, \tag{11}$$

and the critical drag force is

$$\tau_c=\rho U_{*c}^2. \tag{12}$$

The Shields number (relative drag force) θ is defined as

$$\theta=\frac{\tau}{g\left(\rho_s-\rho\right)d}, \tag{13}$$

and the critical Shields number is

$$\theta_c=\frac{\tau_c}{g\left(\rho_s-\rho\right)d}. \tag{14}$$

In eqs. (11)–(14), U_* is the friction velocity, U_{*c} is the critical friction velocity, ρ_s is the sand density, g is the gravity acceleration and d is the mean sediment diameter.

The sediment transport rate formula described by Engelund and Fredsoe [22] was chosen for the current model:

$$q_b=\rho_s\frac{\pi}{6}d^3\frac{1}{d^2}u_b p, \tag{15}$$

where q_b is the bed-load transport rate in unit time and unit width. u_b is the mean transport velocity of bed-load, and p is the probability that all particles in a single layer will be in motion. As shown in eq. (15), the bed-load transport rate is determined only by u_b and p for particular sediment.

The driving force on a single particle is

$$F_D=C_D\frac{\pi}{4}d^2\rho\frac{\left(aU_*-u_b\right)^2}{2}. \tag{16}$$

The friction force is

$$f_D=\left(\gamma_s-\gamma\right)\frac{\pi d^3}{6}\beta. \tag{17}$$

The driving force is equal to the friction force, so we can deduce

$$\frac{u_b}{U_*}=a\left(1-\sqrt{\frac{4\beta}{3a^2C_D\theta}}\right), \tag{18}$$

which can be simplified when $\theta_0=\dfrac{4\beta}{3a^2C_D}$ as

$$\frac{u_b}{U_*}=a\left(1-\sqrt{\frac{\theta_0}{\theta}}\right), \tag{19}$$

where C_D is the coefficient of the driving force, and aU_* is the water velocity where bed-load sand is moving. In the zone near the bed, a = 6–10. When $\theta=\theta_0$, $u_b=0$. In other words, θ_0 is equivalent to the relative drag force that prevents sediment from moving; therefore, θ_0 is less than the critical relative drag force θ_c. Eq. (20) is then obtained by rewriting eq. (19):

$$\frac{u_b}{U_*}=a\left(1-0.7\sqrt{\frac{\theta_c}{\theta}}\right). \tag{20}$$

The drag force is the sum of the critical drag force acting on the sandy bed and the drag force acting on the moving sediment particles, which is described as follows:

$$\tau=\tau_c+n\left(\gamma_s-\gamma\right)\frac{\pi d^3}{6}\beta, \tag{21}$$

where n is the quantity of sediment particles. The relationship between the quantity of sand particles in the unit bed area $\left(1/d^2\right)$ and the probability for sand moving (p) is $p=n\Big/\left(\frac{1}{d^2}\right)$. Considering eqs. (13) and (14), we can get the following expression for p:

$$p=\frac{6}{\pi\beta}\left(\theta-\theta_c\right). \tag{22}$$

As mentioned above, u_b and p are the two determined factors of the bed-load transport rate q_b. By substituting the u_b and p obtained from eqs. (20) and (22) into eq. (15), respectively, the formula describing the bed-load sediment transport rate is deduced as follows with the dynamic friction coefficient $\beta=0.8$ and the constant $a=9.3$:

$$q_b=\begin{cases}11.6\rho_s d\left(\theta-\theta_c\right)\left(\sqrt{\theta}-0.7\sqrt{\theta_c}\right)\\ \times\sqrt{\dfrac{\rho_s-\rho}{\rho}gd}, & \theta\geqslant\theta_c,\\ 0, & \theta<\theta_c,\end{cases} \tag{23}$$

which is the bed-load model used in this paper. Eqs. (20), (22) and (23) show that for certain sediments, the bed-load model is primarily determined by Shields number. The scour occurs in beds where the Shields number reaches the critical Shields number.

In general, the critical Shields number for a horizontal bed is taken as $\theta_{c0}=0.04$, while for a sloped bed the critical Shields parameter is adjusted according to Allen [23]

$$\theta_c=\theta_{c0}\left(\cos\alpha-\frac{\sin\alpha}{\tan\phi}\right), \tag{24}$$

where ϕ is the repose angle of the sediment, and α is the slope angle between the sand bed and the flat plane. This approach takes both the local slope of the bed and the local shear force direction into consideration. Eq. (24) was also used by Liang and Cheng [11].

3.2 Morphologic model

Zhao et al. [16] developed a morphologic model in which the scour hole profile evolution was simulated by solving the mass conservation equation of the sediment:

$$\frac{\partial Y_b}{\partial t}=-\frac{1}{1-\lambda_s}\frac{\partial q}{\partial X}, \tag{25}$$

where Y_b is the sandy bed level, λ_s is the porosity of the sediment, and q is a sediment transport rate including bed-load and suspended-load. Only bed-load was taken into consideration in this study; therefore, the q in eq. (25) is equal to the q_b in eq. (23). To ensure that the bed slope angle in the scouring process does not exceed the repose angle of sand, a sand slide model developed by Liang et al. [11] was employed in this study. The computational mesh in the entire domain updates when a new location of the nodal points at the interface is known after each time step of the interface elevation change. According to a study conducted by Liu et al. [15], the mesh deformation is controlled by the following equation:

$$\nabla\cdot(\eta\nabla S_i)=0, \tag{26}$$

where η is a diffusion coefficient that controls the mesh deformation and is set to $\eta=1/A$, where A is the area of the cell required to avoid excessive deformation. For different cells, the coefficient η is different. S_i is the displacement of the nodal point in i direction. Because the computational mesh is constantly updated with the development of scouring, the governing equations for fluid and sediment are solved on the continuously changing mesh.

4 Model validation

4.1 Flume experiment

The experimental set in this study is shown in Figure 1. The glass flume used was 910 mm long, 300 mm wide and 500 mm high. With the flume bottom elevation as benchmarks, the initial bed level was 90 mm and the fluid height was 240 mm. Upstream and downstream overflow baffles are used to keep the water height constant. The water used in this experiment was supplied by a water tank with constant water head. Seven experimental series were conducted using a jet nozzle width of $2b_0=2.5$ mm and an impinging distance of $h=117$ mm. At the nozzle, the jet velocities were

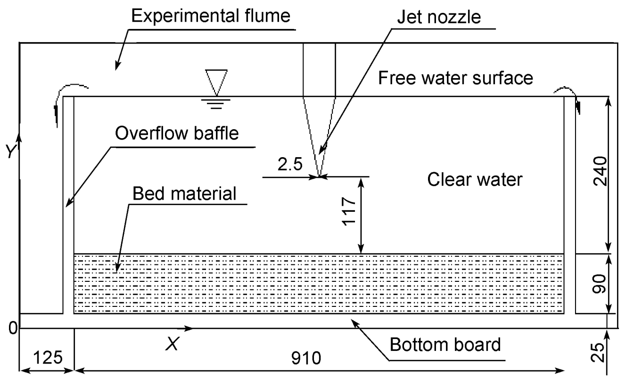

Figure 1 Experimental setup (mm).

changed by adjusting the flow valve. In this flume experiment, the flow was adjusted from 0–4 m³/h. The sand used here was uniformly non cohesive with a density $\rho_s =$ 2650 kg/m³, a median size of $d = 2$ mm and a porosity $\lambda_s = 0.5$, the repose angle of the sediment is $\varphi = 45°$, the critical Shields number for a horizontal bed is $\theta_{c0} = 0.04$.

4.2 Numerical simulation

The computational domain was the same as the experimental setup (see Figure 1). The pressure boundary conditions were used for both the upstream and downstream boundaries and the velocity inlet boundary condition was set at the jet nozzle, while the moving boundary condition as well as a wall function was used at the water-sediment interface. The computational domain was discretized with a total of 48024 non-structured 2D cells.

4.3 Validation

4.3.1 Scour development with time

The dimension of a scour hole in a stable state, such as the maximum scour depth and dune height, is always considered by engineers. To understand the law of jet scour, investigation of the evolution of the scour hole is important. In this experiment, measured values of the scour hole were obtained, as well as some photos of the scour hole at different times. During the numerical simulation, the moving mesh method was employed to model the scour profile throughout the evolution process. The evolution of the scour hole when the jet nozzle velocity was 1.5 m/s is shown in Figure 2. As shown in the figure, the numerical simulation results were in good agreement with the experimental results.

From *t*=0 s to *t*=42 s, the scour hole changed from shallow to deep. However, at a certain depth (*t*=42 s), scouring in the vertical direction became slow. After *t*=42 s, the main part of the jet began to oscillate, which caused strong turbulence in the scour hole.

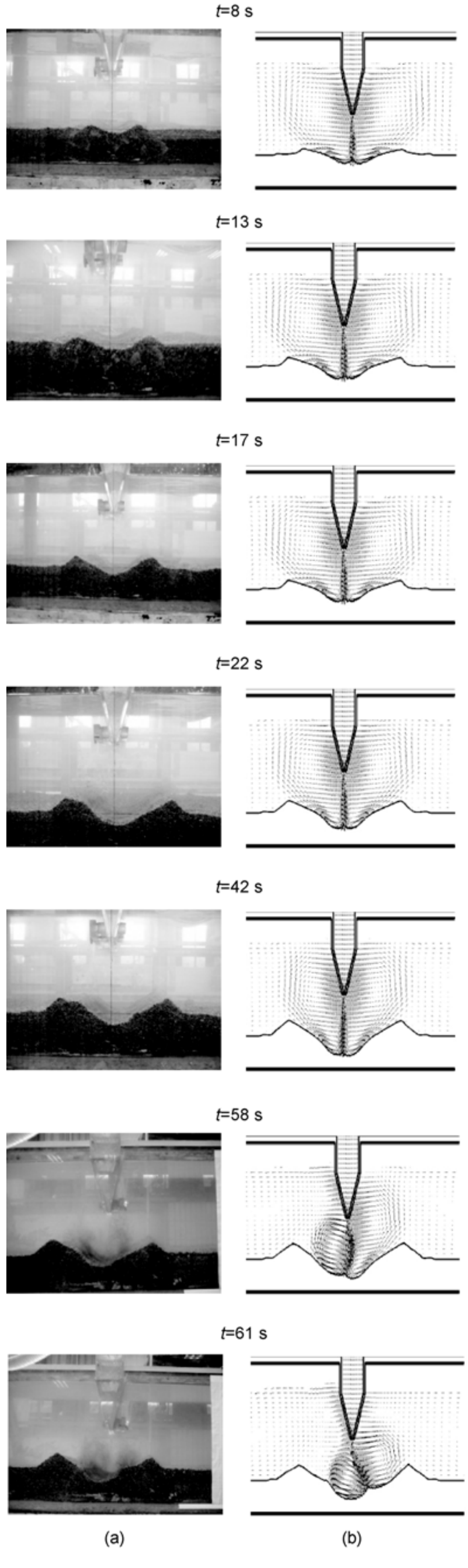

Figure 2 The time evolution of the scour hole of experiment (a) and simulation (b).

Both the experimental and simulated results suggested that the evolution process of the scour hole resulting from the 2D submerged jet occurred in three main stages. In the first stage, from *t*=0 s to *t*=22 s, scour in the vertical direction developed rapidly and two dunes formed quickly. In the second stage, from *t*=22 s to *t*=42 s, the vertical scour developed slowly with the main part of the jet being stable. In the last stage, after *t*=42 s, the main part of the jet started to oscillate, the stagnation point started to move and the jet scour reached dynamic equilibrium. Because the sand slide model was used, the slope of the scour profile did not exceed the angle repose of sediment under stable or oscillating conditions.

The simulated results show that the stagnation point at the bottom of the scour hole was obvious. After the jet impinged the stagnation point at the sand bed, it was divided into two parts flowing in opposite directions along the sand bed. The streamline then turned sharply at that stagnation point.

4.3.2 *Flow characteristics in the scour hole*

The oscillation phenomenon was captured experimentally and by simulation. When the scour hole reached the maximum depth, the jet started to oscillate, resulting in more complex flow and sediment movement in the scour hole. In this study, three typical flow patterns for the case of 1.5 m/s jet velocity at the nozzle outlet were selected to illustrate the flow characteristics. When *t*=39 s, the jet remained stable, the scouring reached the maximum depth and the flow field and scour hole were symmetrically distributed along the centerline of the jet. At *t*=45 s and *t*=53 s the oscillation moved from one side to the other.

Based on the theory of impinging jet, the flow field can be divided into three areas: the free jet area, impact jet area and attached wall jet area (Figure 3). In the free jet area, the jet diffuses and the momentum exchanges dramatically with the surrounding water. In the impinging jet area, the main streamline turns sharply and the flow direction changes when the jet reaches that stagnation point, the velocity decreases and the dynamic pressure increases. In the attached wall jet area, the main part of the jet is divided into two parts overflowing the dunes outside the scour hole along the water-sand interface.

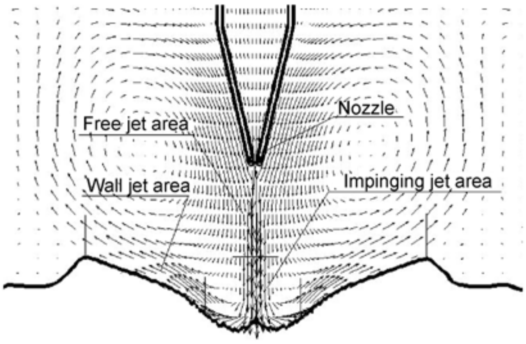

Figure 3 Schematic diagram of jet flow.

At *t*=39 s, the jet was stable and the scour hole and the distribution of the hydraulic elements were symmetrical (Figures 4–7). There were two symmetrical vortexes in the low velocity zones surrounded by the incident flow and the reflected flow. The turbulent kinetic energy k and the turbulent dissipation rate ε are two important parameters that reflect the transfer of energy between the pulsating flow field and the time-averaged one. Relatively large values of the velocity gradient, the turbulent kinetic energy k and the turbulent dissipation rate ε were observed in the main part of the jet and the bottom of the scour hole, where the main energy exchange between the jet and the water and between the water and the sand occurred, as shown in Figures 6 and 7.

When the jet started to oscillate from side to side, the movements of the water and the sand in the scour hole became complex, and the vortexes, the scour holes and the hydraulic elements were no longer symmetrical, but were oscillating (see *t*=45 s and *t*=53 s in Figures 4–7).

Based on the above analysis, the flow field of the jet scour was different from that of the free submerged jet or the impinging jet. The energy exchange primarily occurred in the main part of the jet and the scour hole.

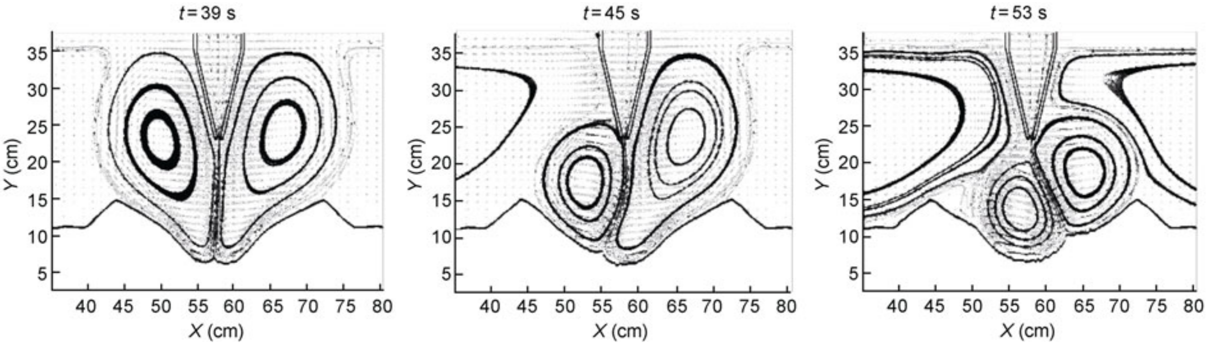

Figure 4 Velocity vectors and streamlines.

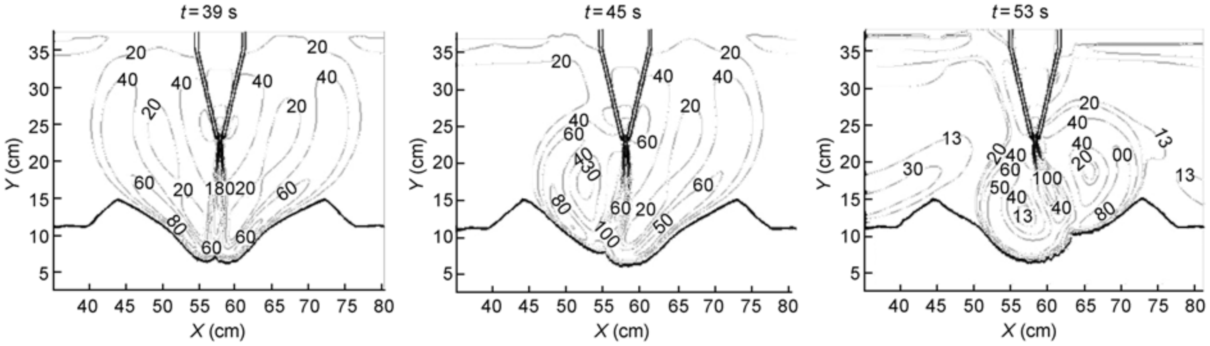

Figure 5 Velocity contours.

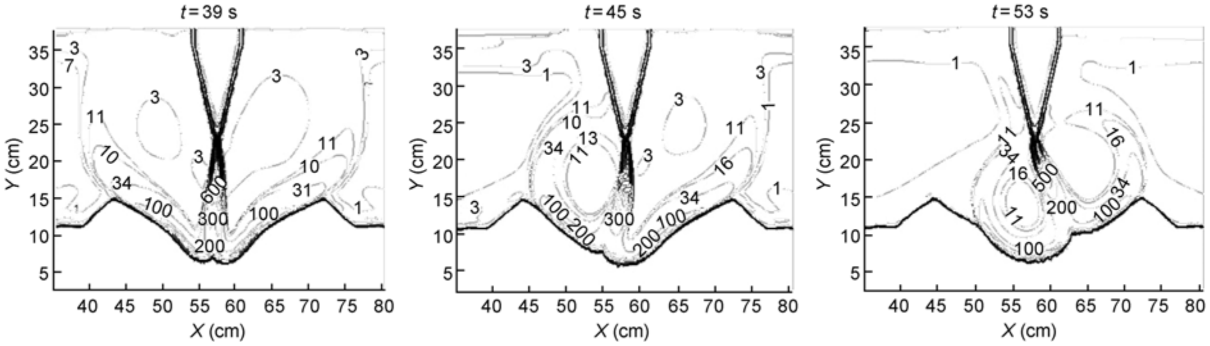

Figure 6 Contours of *k*.

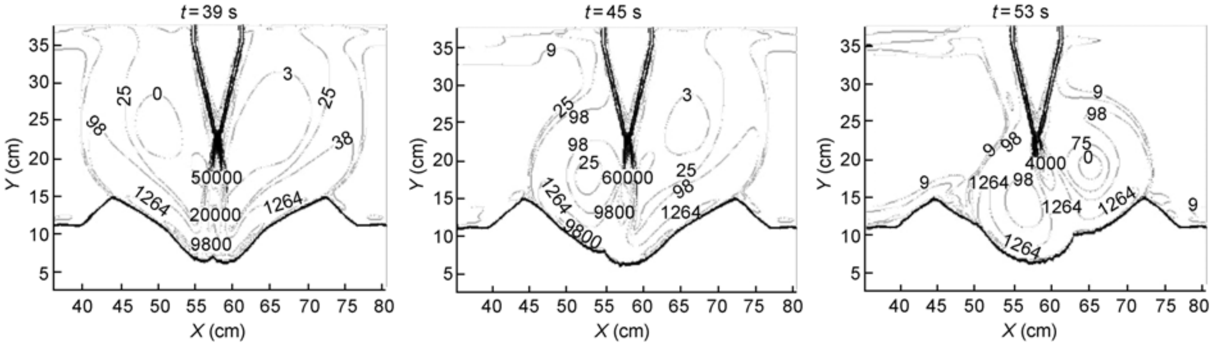

Figure 7 Contours of ε.

5 Results and analysis

5.1 The jet velocity at the nozzle

In the experiment, five cases corresponding to five different jet velocities were considered. The characteristic dimensions of the scour hole were obtained when the jet was stable. For each case, the characteristic dimensions included the maximum depth $\varepsilon_{m\infty}$, the radius at the initial bed $r_{m\infty}$, the radius at half of the maximum depth b_{∞}, the dune height Δ_{∞}, the distance between the centerline and the dune inner point at half of the dune height $b_{2\infty}$, the distance between the centerline and the dune peak $r_{c\infty}$ and the distance between the centerline and the external point at the initial bed r_{∞} (see Figure 8).

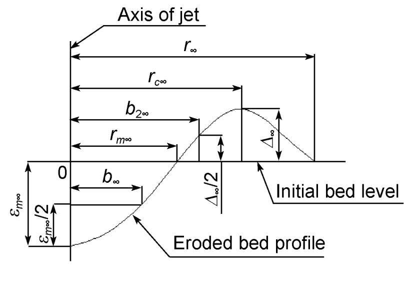

Figure 8 Characteristic dimensions of scour hole.

As mentioned above, the scour hole was symmetrical about the centerline when the jet was stable, so only the right half of the scour hole is shown. The experimental results are shown in Table 2 and the simulated results in Table 3.

Figures 9 and 10 show the scour hole profiles obtained experimentally and by simulation, respectively. In the experiments, the initial bed level was Y=11.5 cm and the jet velocities at the nozzle gradually increased from 0.74 to 1.5 m/s, which was the maximum jet velocity at the nozzle outlet.

Figure 9 shows that the scouring region increased as the jet velocity increased at the nozzle. The results shown in Table 2 reveal that there was an increase in the characteristic dimensions with the jet velocity. Figure 10 shows the computational results, in which the jet velocities gradually increased from 0.9 to 3.0 m/s to expand the velocity region of the experiment. The same conclusion can be drawn from the data presented in Figure 10.

5.2 The geometrical similarity of the scour hole

Li [2] reported that the geometrical similarity of the scour hole indicates that the dimensionless scour profiles are the same. With dimensionless coordinates, the scour profiles at each moment were the same, and the scour profiles were the same for all cases using the same sand. Considering the symmetry, only the right half of the scour hole was displayed to illustrate its geometrical similarity. A new coordinate system was introduced in this study, in which the x-axis is the initial interface and the y-axis is the centerline (see Figure 8). With the distance $r_{c\infty}$ as the dimensionless parameter, Figures 11 and 12 show the geometrical similarity between the experiment and the simulation, respectively. The scour profiles were similar for the five different cases in the experiment, as well as for the eight cases in the simulation. Using the same sand in the experiment and simulation resulted in the dimensionless scour profiles shown in

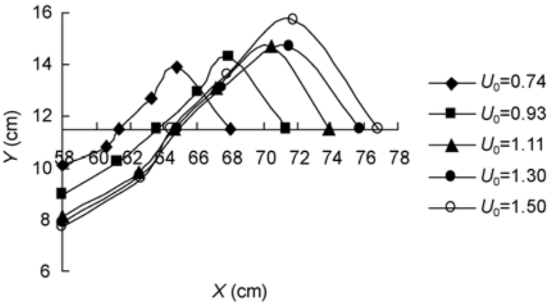

Figure 9 Scour profiles (experiment).

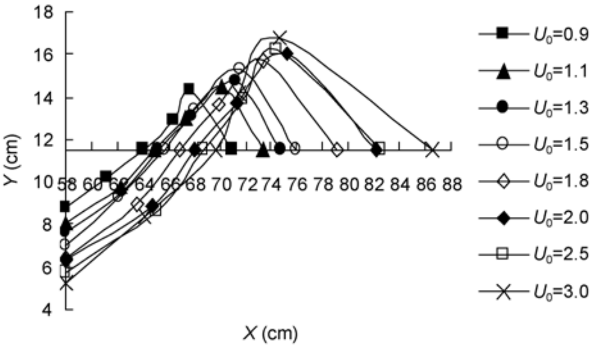

Figure 10 Scour profiles (simulation).

Table 2 Experimental data of characteristic dimensions

U_0 (m/s)	Characteristic dimension (cm)						
	$\varepsilon_{m\infty}$	Δ_∞	b_∞	$r_{m\infty}$	$r_{c\infty}$	r_∞	$b_{2\infty}$
0.74	1.4	2.4	2.6	3.4	6.8	10.0	5.3
0.93	2.5	2.8	3.3	5.6	9.9	13.4	8.1
1.11	3.4	3.2	4.5	6.6	12.4	15.9	9.2
1.30	3.6	3.2	4.6	6.9	13.5	17.7	9.5
1.50	3.8	4.2	4.7	6.5	13.8	18.8	9.8

Table 3 Simulated data characteristic dimensions

U_0 (m/s)	Characteristic dimension (cm)						
	$\varepsilon_{m\infty}$	Δ_∞	b_∞	$r_{m\infty}$	$r_{c\infty}$	r_∞	$b_{2\infty}$
0.9	2.7	2.8	3.2	6.0	9.7	13.0	8.4
1.1	3.5	3.0	4.3	6.8	12.2	15.3	9.3
1.3	3.9	3.2	4.4	7.2	13.2	16.8	9.8
1.5	4.5	3.8	4.6	7.7	13.6	17.9	10.0
1.8	5.1	4.2	5.7	8.9	15.3	21.2	11.9
2.0	5.2	4.5	6.3	10.0	17.3	24.2	13.3
2.5	5.8	4.7	6.9	10.8	16.4	24.6	13.8
3.0	6.3	5.3	7.4	11.7	16.7	28.6	13.5

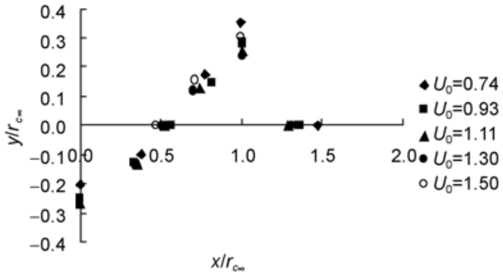

Figure 11 Non-dimensional scour profiles (experiment).

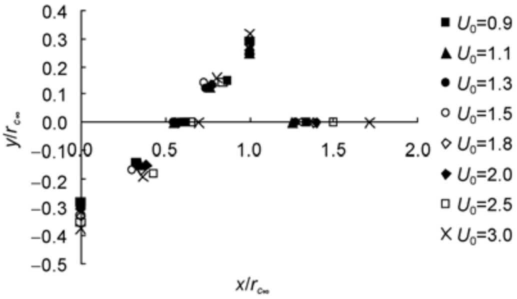

Figure 12 Non-dimensional scour profiles (simulation).

Figures 11 and 12 being almost the same. The mathematical model was also validated by the consistent results.

5.3 The characteristic length of the scour hole

Rajaratnam [8] used dimensional analysis to deduce the semi-experience formula of the characteristic length of the scour hole. Using the velocity formula at the jet centerline according to ref. [1], the centerline velocity of the jet at the level of the initial bed (see Figure 1) can be calculated as follows:

$$U_0' = 2.37U_0\sqrt{\frac{2b_0}{h}}, \tag{27}$$

where U_0 and $2b_0$ are the velocity and width of the jet at the nozzle, and h is the impinging distance. The density Froude number is defined by

$$F_{\rm rd}' = \frac{U_0'}{\sqrt{g\frac{\Delta\rho}{\rho}d}}. \tag{28}$$

The influencing factors of the jet are the jet characteristic, fluid characteristic and the sand characteristic. The characteristic length of the scour hole during the equilibrium state is expressed by

$$l = f(U_0', 2b_0, \rho, \nu, g, \Delta\rho, d), \tag{29}$$

in which l is the characteristic length, ν is the kinetic viscosity, and $\Delta\rho = \rho_s - \rho$. Scaled with the jet width $2b_0$ at the nozzle, the dimensionless expression is

$$\frac{l}{2b_0} = f\left(\frac{U_0'}{\sqrt{g\frac{\Delta\rho}{\rho}d}}, \frac{\nu}{\sqrt{g\frac{\Delta\rho}{\rho}d^3}}\right), \tag{30}$$

where $l/2b_0$ is the relative scour length. In this study, the water temperature was constant, so ν was a constant. As a result, eq. (30) is simplified to

$$\frac{l}{2b_0} = f(F_{\rm rd}'). \tag{31}$$

These calculations show that the main dimensions of the scour hole at equilibrium are a function of the density Froude number, $F_{\rm rd}'$, which is only determined by the centerline velocity of the jet U_0' at the initial time.

In Figure 13, the relative scour depth $\varepsilon_{m\infty}/(2b_0)$ is plotted against the density Froude number $F_{\rm rd}'$. Figures 14 and 15 show the influences of $F_{\rm rd}'$ on $r_{m\infty}/(2b_0)$ and $\varDelta_\infty/(2b_0)$, respectively. As shown in Figures 13 and 14, when the jet velocity at nozzle U_0 was in the region from 0.9 to 1.5 m/s, the calculated results and the experimental results were in the same region and had the same developmental tendency. These experimental results were validated by the calculated ones. Therefore, it is reasonable to take the computational results as the extension of the experimental ones. The results revealed that the dimensionless scour length could be estimated using the following equations:

$$\frac{\varepsilon_{m\infty}}{2b_0} = 13.27\ln F_{\rm rd}' + 2.76, \tag{32}$$

$$\frac{r_{m\infty}}{2b_0} = 21.51\ln F_{\rm rd}' + 8.87, \tag{33}$$

$$\frac{\varDelta_\infty}{2b_0} = 8.37\ln F_{\rm rd}' + 6.26. \tag{34}$$

The three correlation coefficients in order were 0.963, 0.934 and 0.955, indicating that the fitted curves agree very well with the scatters and that eqs. (32)–(34) can be used as semi-empirical formulas to describe the scour hole. Eqs. (32)–(34) also indicate that the dimensionless characteristic

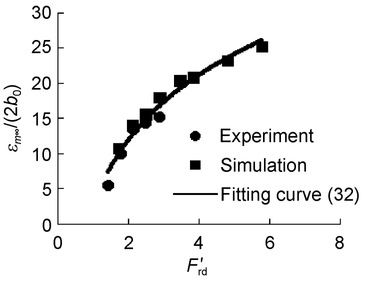

Figure 13 Non-dimensional scour depths.

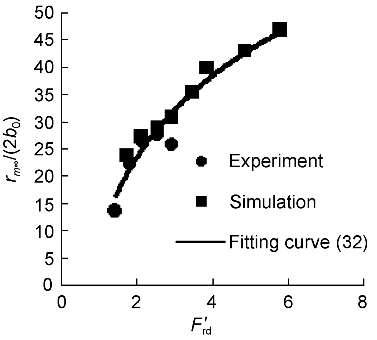

Figure 14 Non-dimensional radii.

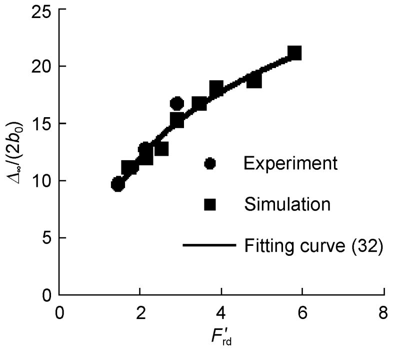

Figure 15 Non-dimensional dune heights.

length of the scour hole is primarily determined by the density Froude number, which is the same as that used in dimensional analysis. This conclusion is similar to those in refs. [6–8]. Eqs. (32)–(34) are all logarithmically related, which illustrates the geometric similarity.

6 Conclusions

In this study, the local scour by vertical submerged jet was simulated using the 2-D RNG k–ε model and moving mesh. Based on the bed-load transport equations and sand slide model, a sediment model was deduced, in which the Shields number is the major parameter. The new sediment model was then used to simulate the bed deformation. The main conclusions can be summarized as follows.

1) The mathematical models and numerical methods used in this study can simulate the process of jet scour of a sandy bed very well.

2) The plane 2-D vertical jet scour process can be divided into three stages. In the first stage, the scour in the vertical direction develops rapidly and the two dunes form quickly. In the second stage, the vertical scour develops slowly and the main part of the jet is stable. In the last stage, the main part of the jet starts to oscillate periodically, and the jet scour eventually reaches dynamic equilibrium.

3) For different cases using the same sand, the scour holes showed geometric similarity, which is similar to the results of previous studies.

4) Based on the mechanical analysis of jet and jet scour, the expressions describing the characteristic length of the scour hole were deduced using dimensional analysis. The semi-experience formulas are given according to computational and experimental results.

This work was supported by the National Natural Science Foundation of China (Grant Nos. 10972163, 51079106)) and the Fundamental Research Funds for the Central Universities (Grant Nos. 2104001, 2103002).

1 Yu C Z. Turbulent Jet (in Chinese). Beijing: Higher Education Press, 1993
2 Li W X. Experiments of scour caused by a wall jet (in Chinese). J Sediment Res, 1995, 4: 50–59
3 Li W X, Li C L. Analysis of local sour caused by a two-dimensional wall jet (in Chinese). J Sediment Res, 1996, 4: 62–68
4 Westrich B, Kobus H. Erosion of a uniform sand bed by continuous and pulsating jets. Proc IAHR Congress, 1973. 91–98
5 Mih W C, Kabir J. Impingement of water jets on non-uniform stream bed. J Hydraul Eng, 1983, 109, 4: 536–548
6 Aderibigbe O O, Rajaratnam N. Erosion of loose beds by submerged circular impinging vertical turbulent jets. J Hydraul Res, 1996, 34: 19–33
7 Aderibigbe O. Effect of sediment gradation on erosion by plane turbulent wall jets. J Hydraul Eng, 1998, 124: 1034–1042
8 Rajaratnam N, Mazurek K A. Erosion of sand by circular impinging water jets with small tailwater. J Hydraul Eng, 2003, 129: 225–229
9 Yüksel A C, Elikoglu Y C, Evik E, et al. Jet scour around vertical piles and pile groups. Ocean Eng, 2005, 32: 349–362
10 Li F J, Cheng L. Numerical model for local scour under offshore pipelines. J Hydraul Eng, 1999, 125: 400–406
11 Liang D F, Cheng L, Li F J. Numerical modeling of flow and scour below a pipeline in currents. Part II: Scour simulation. Coast Eng, 2005, 52: 43–62
12 Salaheldin T M, Imran J, Hanif C M. Numerical modeling of three-dimensional flow field around circular piers. J Hydraul Eng, 2004, 130: 91–100
13 Roulund A, Sumer B M, Fredsoe J, et al. Numerical and experimental investigation of flow and scour around a circular pile. J Fluid Mech, 2005, 534: 351–401
14 Lu L, Li Y, Qin J. Numerical simulation of the equilibrium profile of local scour around submarine pipelines based on renormalized group turbulence model. Ocean Eng, 2005, 32: 2007–2019
15 Liu X, García M H. Three-dimensional numerical model with free water surface and mesh deformation for local sediment scour. J Waterway, Port, Coast, Ocean Eng, 2008, 134: 203-217
16 Zhao M, Cheng L. Numerical modeling of local scour below a piggyback pipeline in currents. J Hydraul Eng, 2008, 134: 1452–1463
17 Yüksel O A, Yüksel Y I. Simulation of a 3D submerged jet flow around a pile. Ocean Eng, 2010, 37: 819–832
18 Li F J, Cheng L. Prediction of lee-wake scouring of pipelines in currents. J Waterway, Port, Cast, Ocean Eng, 2001, 127: 106–112
19 Yakhot V, Orszag S A. Renormalization group analysis of turbulence. I. Basic theory. J Sci Comp, 1986, 1: 3–51
20 Chen B. The numerical simulation of local scour in front of a vertical-wall breakwater. J Hydrodynam Ser B, 2006, 18: 134–138
21 Zhang R J. River Sediment Dynamics (in Chinese). Beijing: China Water Power Press, 1998
22 Engelund F, Fredsoe J. A sediment transport model for straight alluvial channels. Nord Hydrol, 1976, 7: 293–306
23 Allen J. Simple models for the shape and symmetry of tidal sand waves: (1) statically stable equilibrium forms. Marin Geol, 1982, 48: 31–49